Combined Inversion of Airborne Electromagneticand Static Magnetic Field Data

Markku Pirttijärvi[1][*], Mohammed A. Zaher[2] and Toivo Korja[3]

[1]Department of Physics and Chemistry, University of Oulu, Finland
[2]National Research Institute of Astronomy and Geophysics, Cairo, Egypt
[3]Oulu Mining School, University of Oulu, Finland

[*]Corresponding author markku.pirttijarvi@gmail.com

Abstract

The frequency domain airborne electromagnetic (AEM) data of the Geological Survey of Finland (GTK) is transformed into apparent resistivity because it's geologically and physically more meaningful and easier to comprehend than the in-phase and quadrature component of the original data. The traditional transformation method based on a model of homogeneous conductive half-space has two main problems: a) conductive sediment layers makes the bedrock appear more conductive and b) the sign-reversals of the in-phase component due to magnetized rocks that cannot be modelled without taking the magnetic susceptibility (or permeability) into account. We present a combined inversion method designed for the AEM and magnetic profile data of GTK. The inversion method uses a two-layer model for AEM data and a stack of vertical magnetized prisms for magnetic data. Laterally constrained inversion is used where the parameter variations between neighbouring points are minimized together with data misfit. We show that it is possible to resolve the four unknown model parameters (resistivity and thickness of the overburden, resistivity and magnetic susceptibility of the basement) even from single frequency AEM data. Moreover, we show that the combined inversion yields improved estimates for bedrock resistivity. In addition to the conductance of the overburden and the resistivity of bedrock, the combined inversion gives realistic estimates for magnetic susceptibility allowing cross-correlation of the sources of conductivity and magnetic anomalies. The efficacy of the inversion method is demonstrated using GTK's airborne data from two example areas

Keywords: airborne geophysical data; electromagnetic data, magnetic data; apparent resistivity; linearized inversion; joint inversion

1   Introduction

Between 1972 and 2008, Geological Survey of Finland (GTK) carried out systematic low altitude airborne geophysical mapping of Finland using a nominal flight altitude of 30 m and line separation of 200 m (*Korhonen*, 2005). The "three-in-one" system of GTK measured the intensity of magnetic (total) field, radioactivity (K, U, Th and total intensity) and the frequency domain electromagnetic (EM) response of a horizontal coil system (*Hautaniemi et al.*, 2005). Over the years, the coil configuration, coil spacing and the frequencies of the EM system have changed (*Hautaniemi et al.*, 2005). At

first (1972–1980), a Douglas DC-3 airplane and horizontal coaxial coil system was used (coil spacing L= 26.5 m, frequency f= 3220 Hz). After 1980, a co-planar horizontal coil system (L= 21.4 m, f= 3113 Hz) was attached to the wing-tips of the De Havilland Twin Otter. Second frequency was introduced in 1995 (f= 3125 and 14368 Hz) and, in 2000, an auxiliary plane, Cessna Caravan, was introduced (L= 17 m, f= 3000 and 14400 Hz). In 2005, after the co-operation with the British Geological Survey started, the number of frequencies was raised to four (f = 912, 3005, 11962, 24510 Hz) (*Leväniemi et al.*, 2009).

Apparent resistivity has traditionally been used to represent the AEM data in a form that is geologically more meaningful than the original measured data, which in the case of frequency domain systems are usually defined as the in-phase (real) and quadrature (imaginary) component. Apparent resistivity is also useful because it 1) compensates for the effects of flight altitude variations, and 2) makes the measurements made on different map sheets comparable for the changes in coil configuration and coil spacing and, to some degree, small changes in the frequency. To compute the apparent resistivity, a half-space model is assumed and such values of resistivity and depth to the half-space are sought for that the model response fits the measured in-phase and quadrature data (*Fraser*, 1978; *Peltoniemi*, 1982). For the AEM data of GTK, the apparent resistivity has been computed using a two-dimensional (2-D) interpolation of transformation tables (*Pirttijärvi*, 1995). Alternatively, apparent resistivity and depth can be computed by numerical inversion. Because these methods are based on non-magnetic conductive half-space, the effects of conductive overburden and magnetic susceptibility are not taken into account. Although magnetic susceptibility (or magnetic permeability) can be included both into lookup table methods (*Beard*, 2000) and in the inversion of permeable conductive half-space (*Huang and Fraser*, 1998 and 2000), we believe that inversion for the parameters of permeable two-layer earth model can produce better apparent resistivity maps, despite the fact that the inversion results tend to be affected by the choice of a starting model (*Beard*, 2000; *Huang and Fraser*, 2003).

To separate the overburden from the basement we will consider a two-layer earth model and use linearized inversion to solve the resistivity and thickness of the overburden and the resistivity of the basement. We limit ourselves to a two-layer model because GTK AEM data has been measured mostly at a single frequency of about 3000 Hz. To improve the solution of the under-determined problem (three unknowns vs. two data values) laterally constrained inversion is used where the parameter variations between neighbouring points are minimized together with data misfit. To account for the high magnetic susceptibility which often in practice gives rise to negative in-phase anomalies we also invert the magnetic susceptibility (permeability) assigned to the basement layer as the fourth unknown parameter. To improve the inversion, we demonstrate that the combined inversion of AEM and static magnetic field data is possible and greatly improves the susceptibility estimates particularly in areas where magnetic anomalies exist but the in-phase component does not change its sign because of high enough conductivity. Thus, we extend the ideas of *Huang and Fraser* (2003) who also considered the inversion of AEM data to magnetic conductive layered earth. We also choose a bit differ-

ent approach than *Suppala et al.* (2008) who presented a laterally constrained inversion of non-magnetic conductive layered earth utilizing several corrective actions such as the correction of altitude values using topographic digital elevation models and EM data calibration using conductivity estimates from ground measurements. Although, these corrections are essential in accurate inversion, we aim to create a semi-automatic inversion method that can be used to process large datasets, for example an entire 1:100000 map sheet (30 km by 40 km), reasonably fast with a minimal amount of user intervention.

Finnish bedrock does not contain many sedimentary lithological units, and, because of several ice ages, the thickness of the overburden, which consists of resistive tills and conductive sedimentary layers of clays, sands, swamps and lakes and lake sediments, is typically only a few metres thick. Therefore, we can limit ourselves to consider only a two-layer earth where the overburden is non-magnetic and the basement layer represents bedrock that is possibly magnetized. The inversion method has been implemented in a computer program (AEMINV version 1.4) that is designed to process the multiple measurement lines of an entire map sheet simultaneously. The inversion results are interpolated on regular grids and plotted as maps of 1) overburden resistivity, 2) overburden thickness and 3) overburden conductance and 4) basement resistivity, 5) cumulative skin depth, and 6) magnetic susceptibility of the basement. The skin depth, $\delta = (2/\omega\mu\sigma)^{1/2}$, defines the distance over which the intensity of EM plane field becomes $1/e \approx 37\%$ of the original intensity at the surface. The cumulative skin depth takes into account the attenuation both in the overburden and in the basement. If multiple frequencies are available, the cumulative skin depth is computed at the lowest frequency. The regional magnetic field obtained from a separate inversion process is also stored. The usefulness of the method is demonstrated for two selected areas in Finland, the other containing magnetic features and the other containing thick sedimentary overburden.

2   The method

2.1   AEM modelling

Frequency domain electromagnetic (FEM) methods are based on the EM induction where the time varying magnetic field generated by the (sinusoidal) current of the transmitter (Tx) loop generates currents in the subsurface conductors. These currents in turn generate a secondary EM field which adds up in the total magnetic field measured as a voltage or current in the receiver (Rx) loop. Various Tx-Rx configurations where the loop orientation and position is different with respect to loops themselves and with the profile direction have been developed over the decades of geophysical prospecting. In airborne applications usually both the transmitter and the receiver are coils the orientation of the axes of which is perpendicular to the plane of the loops. Figure 1 shows four Tx-Rx configurations where the first two, coaxial and coplanar vertical loop (horizontal coil) systems, have been used in the low-altitude airborne EM mapping of GTK. In case of 1D layered earth, the coplanar horizontal loop (vertical coil) system (Figure

1c), also known as Slingram geometry, gives exactly the same response whether operated in in-line or in broadside mode.
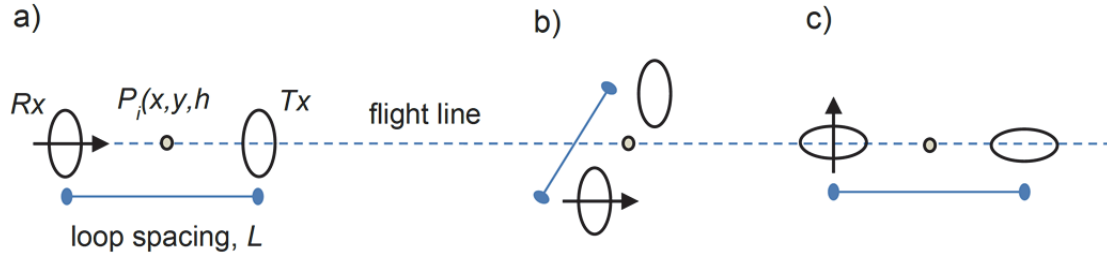

Fig. 1. Schematic view of three loop configurations commonly used in geophysical EM measurements: a) coaxial and b) coplanar vertical loops (horizontal coils), and c) coplanar horizontal loops (vertical coils). The EM response is positioned at the center $P_i(x,y,h)$ between the transmitter (Tx) and the receiver (Rx), the loop spacing (L) of which is kept constant.

The FEM response is defined as the secondary magnetic field (B_s) normalized with the primary (free space) magnetic field (B_0). Taking into account that the total field is the sum of the primary and secondary field ($B_{tot} = B_s + B_0$) and there is an unknown phase shift between them, the AEM response can be defined as in-phase (real) and out-of-phase (imaginary or quadrature) components:

$$\mathrm{Re} = \left(\frac{\mathrm{Re}(B_{tot})}{B_0} - 1 \right) \times 10^6 \, \mathrm{ppm}, \quad \mathrm{Im} = \left(\frac{\mathrm{Im}(B_{tot})}{B_0} \right) \times 10^6 \, \mathrm{ppm}, \tag{1}$$

where $\mathrm{Re}(B_{tot})$ is the part of the total field that is in the same phase as the primary field and $\mathrm{Im}(B_{tot})$ is the part that has $\pi/2$ phase shift with the primary field. Because of the flight altitude the AEM response is normally defined in parts-per-million (ppm) and ground data is presented in percent (%).

Figure 2a shows the two-layer model used for AEM computations. The four unknown parameters are the resistivity and thickness of the overburden layer (ρ_1, t_1), and the resistivity and magnetic permeability of the basement layer (ρ_2, μ_2). Magnetic permeability is the product of free-space magnetic permeability (μ_0) and relative magnetic permeability (μ_r), which in turn is related to the magnetic susceptibility ($\kappa = \mu_r - 1$) used in the modelling of static magnetic field. The AEM response is computed along the measurement profile at data location $P_i(x,y,h)$ which is the centre point between the transmitter and receiver. The model is one-dimensional, and hence, each data point is computed independently. Therefore, the true x and y coordinates are not needed in the AEM computations, unlike the elevation h.

Figure 2b shows the model used in static magnetic field computations. The model consists of vertical prisms the width of which is based on the intervals between adjacent AEM data points. The depth to the top of the prisms is equal to that of the overburden thickness used in AEM modelling. The strike direction, strike length and depth extent of the prisms are fixed parameters. Unlike in AEM modelling the response is computed as the superposition of the (nearest) underlying prisms, and hence, in addition to the eleva-

tion (h), the horizontal distances (x and y coordinates) between the prisms and the computation point must be taken into account. The coordinates of the magnetic data $P_j(x,y,h)$ are usually different from those of AEM data (P_i), because magnetic field is measured with finer sampling than AEM data (*Hautaniemi et al.*, 2005).
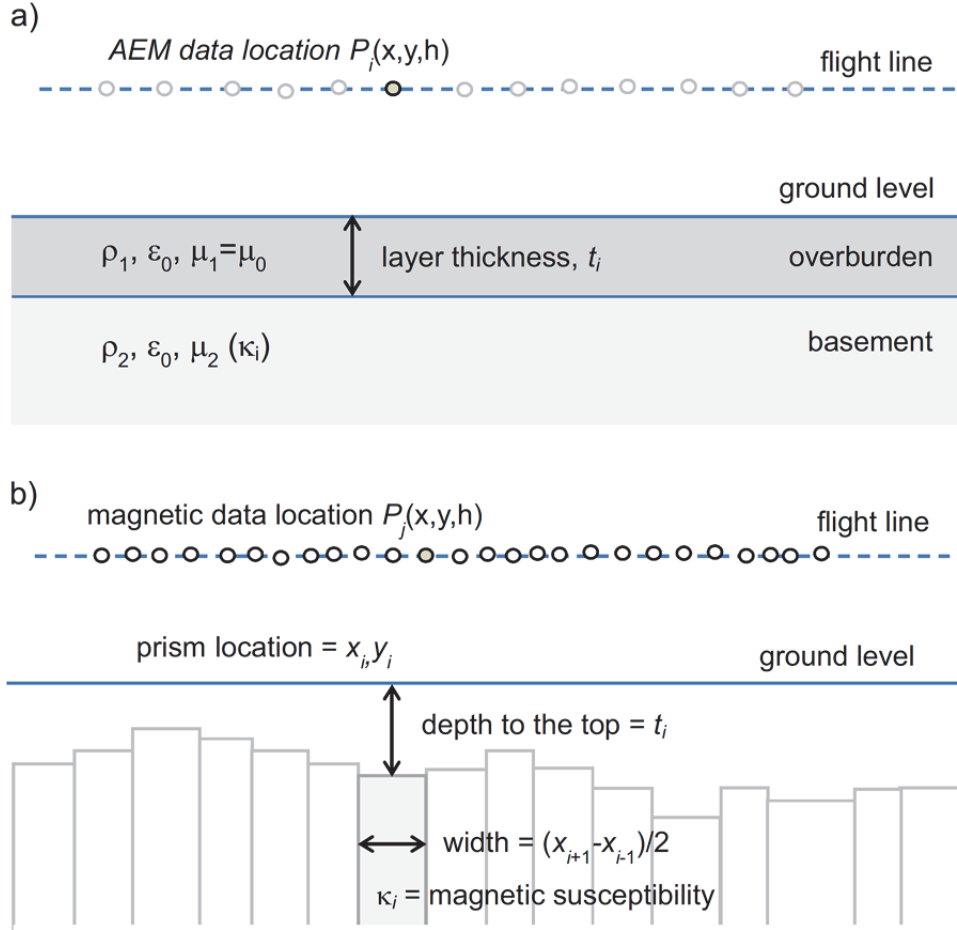
a)
AEM data location P_i(x,y,h)   flight line

ground level

ρ_1, ε_0, $\mu_1=\mu_0$ layer thickness, t_i overburden

ρ_2, ε_0, μ_2 (κ_i)   basement

b)
magnetic data location P_j(x,y,h)   flight line

prism location = x_i,y_i ground level

depth to the top = t_i

width = $(x_{i+1}-x_{i-1})/2$

κ_i = magnetic susceptibility

Fig. 2. Schematic view of a) the two-layer resistivity model and b) the magnetic model used in the joint interpretation of AEM and magnetic data. In AEM modelling each data point P_i is handled assuming a two-layered model beneath that point. In magnetic modelling, the magnetic field is computed as the superposition of the neighboring prism models the width of which is based on the AEM data sampling.

The AEM response of a dipole source and a receiver above layered earth is computed using the solutions presented by *Keller and Frischknecht* (1966) and *Ward and Hohmann* (1988). The solution for coplanar vertical loops (Figure 1b) is (*Keller and Frischknecht*, 1967)

$$\frac{B_s}{B_0} = r^2 \int_0^\infty R(\lambda)\lambda e^{-2\lambda h} J_1(\lambda r)d\lambda \qquad (2)$$

where r is the distance from the source (coil spacing), λ is an integration variable, h is the elevation of the Tx and Rx loops, and J_1 is Bessel function of the first kind of order

one. Likewise the solutions for the vertical coaxial loops (Figure 1a) and horizontal co-planar loops (Figure 1c and 1d) are (*Keller and Frischknecht, 1967*)

$$\frac{B_s}{B_0} = r^2 \int_0^\infty R(\lambda)\lambda e^{-2\lambda h} J_1(\lambda r)d\lambda - r^3 \int_0^\infty R(\lambda)\lambda^2 e^{-2\lambda h} J_0(\lambda r)d\lambda \tag{3}$$

and

$$\frac{B_s}{B_0} = r^3 \int_0^\infty R(\lambda)\lambda^2 e^{-2\lambda h} J_0(\lambda r)d\lambda \tag{4}$$

Function $R(\lambda)$ is the (TE mode) reflection coefficient for a computation point above the ground surface and it can written as (*Ward and Hohmann*, 1988)

$$R(\lambda) = \frac{Y_0 - \hat{Y}_1}{Y_0 + \hat{Y}_1} \tag{5}$$

where Y_1 is the surface admittance and $Y_0 = u_0/(i\omega\mu_0)$ is the intrinsic admittance of free space, where i is the imaginary number ($i^2 = -1$), $\omega = 2\pi f$ is the angular frequency, and μ_0 is the magnetic permeability of the free space. The surface admittance of L-layered earth is computed using a recursive relation (*Ward and Hohmann*, 1988)

$$\hat{Y}_l = Y_l \frac{\hat{Y}_{l+1} + Y_l \tanh(u_l t_l)}{Y_l + \hat{Y}_{l+1} \tanh(u_l t_l)}, \quad l = 1, 2, ..., L \tag{6}$$

where $Y_l = u_l/(i\omega\mu_l)$ and $\hat{Y}_L = Y_L$ in the basement layer, t_l is the thickness and $\mu_l = \mu_0\mu_{rl}$ is the magnetic permeability of the l-th layer, and $u_l = (\lambda^2 + k_l^2)^{1/2}$. Letting us consider that the frequency is low enough we can make a so-called quasi-static approximation ($\omega\sigma << \varepsilon$), and the wave number of the l.th layer becomes $k_l^2 = -i\omega\mu_l\sigma_l$, where σ_l is the conductivity of layer l ($\sigma_l = \rho_l^{-1}$). In the air $k_0 = 0$, and hence $u_0 = \lambda$.

The Hankel transform integrals in Eqs. (2)–(4) are computed using the convolution method and optimized filter coefficients by Christensen (1990). To improve computational stability, distance (r), elevation (h), and layer thickness (t) are normalized with the skin depth of the first layer $\delta = (2/\omega\mu_0\sigma_1)^{1/2}$, and hence, $u_l = (\lambda'^2 + 2i\,\sigma_l/\sigma_1)^{1/2}$, where $\lambda' = \lambda\delta$ is the new integration variable. Additional stabilization to the kernel function is obtained expressing $\tanh(u_l t_l)$ in terms of $\exp(-2u_l t_l)$.

2.2   Magnetic modelling

Although it would suffice to compute the magnetic anomalies using the well-known solution of a thick magnetized 2D sheet (eg. *Parasnis*, 1979) or vertical prism of infinite depth extent (*Bhattacharyya*, 1964) we compute the total magnetic field using solution derived for a 3D dipping prism (*Hjelt*, 1972), because this leaves us an option to model adjacent profiles or gridded data in the future. In the following the total magnetic anomaly is given in rectangular coordinates of the dipping prism, where y axis is

along the strike direction and z axis is positive downwards. The total field anomaly of a dipping prism (dip angle φ) is (*Hjelt*, 1972)

$$\Delta B_t = \Delta B_x \cos I \sin \beta + \Delta B_y \cos I \cos \beta + \Delta B_z \sin I \tag{7}$$

where I is the inclination of earth's magnetic field and β is the azimuth of the strike direction with reference to the geomagnetic north. The components of the magnetic anomaly are (*Hjelt*, 1972)

$$\Delta B_x = \mu_0 \sum_{i=1}^{3} M_i T_{1i} \quad \Delta B_y = \mu_0 \sum_{i=1}^{3} M_i T_{2i} \quad \Delta B_z = \mu_0 \sum_{i=1}^{3} M_i T_{3i} \tag{8}$$

where $M_1 = M_x \sin\varphi - M_z \cos\varphi$, $M_2 = M_y$ ja $M_3 = M_z$ are the components of magnetization perpendicular to the surfaces of the prism. The nine functions T_{ij} are (*Hjelt*, 1972)

$$
\begin{aligned}
T_{11} &= -\sin\varphi \cdot \phi_{1u} + \cos\varphi \cdot \phi_{2v} & T_{12} &= \sin\varphi \cdot \phi_{2w} & T_{13} &= \phi_{2v} \\
T_{21} &= \phi_{2w} & T_{22} &= \phi_{1v} & T_{23} &= \phi_{2u} \\
T_{31} &= \cos\varphi \cdot \phi_{1u} + \sin\varphi \cdot \phi_{2v} & T_{32} &= -\cos\varphi \cdot \phi_{2w} + \phi_{2u} & T_{33} &= -\phi_{1w}
\end{aligned}
\tag{9}
$$

where ϕ are the six solved definite volume integrals

$$\phi_{1u} = \arctan\left[\frac{v(u\cos\varphi + w\sin\varphi)}{u(u\sin\varphi - w\cos\varphi)R} \right]_{u_2 \, v_2 \, w_2}^{u_1 \, v_1 \, w_1} \Bigg| \Bigg| \Bigg| \tag{10}$$

$$\phi_{1v} = \arctan\left[\frac{v^2 \cos\varphi - w(u\sin\varphi - w\cos\varphi))}{v\sin\varphi \cdot R} \right]_{u_2 \, v_2 \, w_2}^{u_1 \, v_1 \, w_1} \Bigg| \Bigg| \Bigg|$$

$$\phi_{1w} = \arctan\left[\frac{vu}{w \cdot R} \right]_{u_2 \, v_2 \, w_2}^{u_1 \, v_1 \, w_1} \Bigg| \Bigg| \Bigg|$$

$$\phi_{2u} = \ln[u + R] \Big|_{u_2 \, v_2 \, w_2}^{u_1 \, v_1 \, w_1} \Bigg| \Bigg| \Bigg|$$

$$\phi_{2v} = \ln[v + R] \Big|_{u_2 \, v_2 \, w_2}^{u_1 \, v_1 \, w_1} \Bigg| \Bigg| \Bigg|$$

$$\phi_{2w} = \ln[u\cos\varphi + w\sin\varphi \cdot R] \Big|_{u_2 \, v_2 \, w_2}^{u_1 \, v_1 \, w_1} \Bigg| \Bigg| \Bigg|$$

where $R=(u^2+v^2+w^2)^{1/2}$ and $u_1= x-x_0-a/2$, $u_2= x-x_0+a/2$, $v_1= y-y_0-b/2$, $v_2= y-y_0+b/2$, $w_1= h-z_0-c$, $w_2= h-z_0$, where (x,y,h) is the computation point and (x_0,y_0,z_0) is the centre of the top of the prism, a is the thickness, b is the width (strike length) and c is the height (depth extent) of the prism.

The thickness of the prism bodies is based on AEM data sampling. The width and height are user-defined parameters (we use $b = 1$ km and $c = 1$ km). The dip and strike direction can be set according to local geology. Since our objective is to process large areas where both the dip and strike are varying, we set dip vertical and the strike direction perpendicular to the profile direction (usually EW or NS). Moreover, the intensity and the direction (inclination and declination) of the inducing magnetic field are computed using the most recent (ver. 11) IGRF model (http://www.ngdc.noaa.gov/IAGA/vmod/igrf.html). The field is computed at the centre of the study area at the year of the measurements.

2.3   Regional magnetic field

The separation of the regional magnetic field, i.e., the local base level due to Earth's inducing magnetic field and the long wavelength trend due to deep and large-scale magnetized sources is essential in magnetic interpretation. We define the regional field using a cubic spline fitted through evenly spaced knot points along the profile. The distance between the knots (Δx_k) is a user defined variable. The smaller the distance is the more accurately the regional field fits the data, and vice versa. Considering the size of the prisms (1 km by 1 km) we set the knot separation larger than that (we use $\Delta x_k = 5$ km). The maximum distance between knots is limited by the condition that there must be at least two knot points on the profile. The initial value of a knot is equal to the smallest measured magnetic field value at range of the nearest knot. This ensures that initially the spline function representing the regional field is located below the measured magnetic field intensity level and there will not appear too many negative magnetic residual anomalies. As we will show later it is necessary that the levels of the knots are optimized during the inversion of two-layer model parameters. Otherwise, the magnetic susceptibility will become overestimated due to many false positive magnetic anomalies.

2.4   Parameter optimization

The parameter optimization is based on iterative linearized inversion with singular value decomposition (SVD) and adaptive damping (*Pirttijärvi et al.*, 2002; *Pirttijärvi*, 2003). The objective is to minimize the difference or misfit ($\mathbf{e}= \mathbf{d}-\mathbf{y}$) between the measured data, $\mathbf{d}= (d_1,d_2,...,d_M)$ and the modelled response $\mathbf{y}= (y_1,y_2,...,y_M)$. Assuming an initial model with parameters $\mathbf{p}= \mathbf{p}_0= (p_1,p_2,..p_N)$, a forward computation is made to yield modelled data vector $\mathbf{y}$ and the sensitivity or Jacobian matrix, A, the elements of which are partial derivatives of the model data with respect to model parameters ($A_{ij} = \partial y_i/\partial p_j$). Although the partial derivatives could be computed more accurately as Hankel transforms (*Huang and Fraser*, 2000) we approximate them as forward differences of

$\log_{10}$-normalized parameters. In addition, we assume that the magnetic anomaly of a prism is a linear function of its magnetic susceptibility, and hence, the sensitivity related to susceptibility is equal to the geometric part of the magnetic anomaly.

The linearization of the problem leads to matrix equation

$$A \cdot \Delta \mathbf{p} = \mathbf{e}.$$ (11)

Solution to Eq. (11) gives an update parameter vector $\mathbf{p}_1 = \mathbf{p}_0 + \Delta \mathbf{p}$. The process is continued iteratively until desired number of iterations has been made and/or the fit between the measured and computed data becomes small enough. The root-mean-square (RMS) error is used as the measure of the data fit

$$RMS_d = \sqrt{\frac{1}{M} \sum_{i=1}^{M} \left(\frac{d_i - y_i}{\Delta d} \right)^2}$$ (12)

where Δd is used to scale the data. The singular value decomposition (SVD) of the Jacobian is (*Press et al.*, 1988)

$$A = U\Lambda V^T,$$ (13)

where U and V are matrices that contain the data eigenvectors and model eigenvectors (T means transpose operation) and Λ is a diagonal matrix that contains the singular values, λ_i. Since both U and V are orthogonal matrices, the solution to Eq. (11) becomes

$$\Delta \mathbf{p} = U\Lambda^{-1}U^T$$ (14)

where the elements of the diagonal Λ^{-1} matrix are simply $1/\lambda_i$. Unfortunately, if some of the singular values are very small the inverse problem becomes ill-posed. Therefore, stabilization or damping is performed by adding a small value, so-called Marquardt factor to the singular values. In practice, the elements of the diagonal Λ^{-1} matrix are multiplied with damping factors (*Hohmann and Raiche*, 1988)

$$t_i = \begin{cases} \dfrac{s_i^4}{s_i^4 + q^4} & s_i \geq q^2 \\ 0 & s_i < q^2 \end{cases}$$ (15)

where $s_i = \lambda_i / \max(\lambda_i)$ are normalized singular values and θ is the relative singular value threshold. Thus, elements of Λ^{-1} that correspond to very small singular values are removed totally and the remaining values are damped so that they never become too small. Damping diminishes the effect of small singular values and the threshold q is used to control the strength of damping.

The constrained inversion is achieved by modifying Eq. (11) so that data misfit ($\mathbf{e}$) is minimized together with the model roughness ($\mathbf{r}$). The roughness is defined as the difference between the parameters (layer resistivity, thickness or susceptibility) from the

mean value of the surrounding points, $\mathbf{r} = \mathbf{p}\text{-}\mathbf{p}^*$. In practice, the roughness (or its recip-rocal, the smoothness) is incorporated by adding the sensitivities of the model rough-ness ($B_{ij} = \partial r_j / \partial p_i$) in the Jacobian and extending the data error vector with the model error $\mathbf{e'}$, which in general is computed against some reference model, but in this case we use a null-model so that $\mathbf{e'} = \mathbf{r}$. Constraining leads to a matrix equation

$$(A + \alpha B)\Delta\mathbf{p} = (\mathbf{e} + \mathbf{e'}) \tag{16}$$

where α is so-called Lagrange scaler or multiplier; a user-defined parameter that em-phasizes either the fit between the data ($\alpha < 1$) or the smoothness of the model ($\alpha > 1$).

3   Results

3.1   Single profile line

The first example considers inversion of AEM data from a single flight line near Iisalmi in Central Finland. The measurement was made in 1986 Twin Otter airplane and coplanar horizontal coil system at the frequency of 3150 Hz and coil spacing of 21.4 m. Five different approaches are used: 1) non-magnetic conductive half-space model and 2) magnetic half-space model and 3) two-layer AEM inversion and 4) two-layer combined inversion of AEM and magnetic data with fixed regional field and 5) two-layer com-bined inversion of AEM and magnetic data with regional field optimization.

The data was first inverted using non-magnetic conductive homogeneous half-space model by optimizing the resistivity and depth to the top of the half-space. Thus, the results shown in Figure 3 resemble the traditional apparent resistivity-depth trans-formation. The initial values of the resistivity and depth were 10000 Ωm and 0 m, re-spectively. The upper graph in Figure 3 shows the measured (dotted lines) and comput-ed (solid lines) in-phase (real) and quadrature (imag) data as dashed red and green lines. The lower graph in Figure 3 shows the resistivity pseudo-section obtained from one-layer inversion. Figure 3 reveals that without magnetic properties the inversion cannot model the negative in-phase values near the beginning at the profile and between 26–40 km. Although, the one-layer model fits the data between 12–17 km where the quadra-ture component is much larger than the in-phase component, the interpreted resistivity value of the host medium is likely to be overestimated because of conductive overbur-den. Another feature in Figure 3 is that in many places the depth to the top of the base-ment is interpreted to be less than flight altitude, and hence, the (resistive) half-space is located above the ground level (z <0 m).
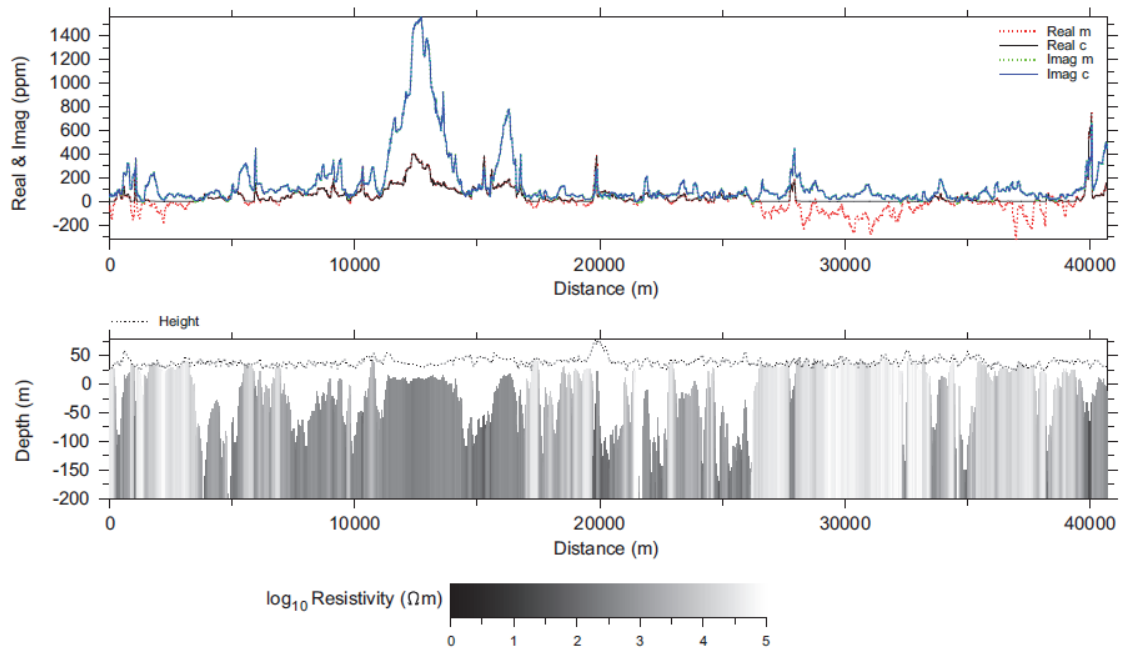
Fig. 3. Inversion results for the non-magnetic conductive half-space model. Upper panel: in-phase (real) and quadrature (imag) components of the measured (dotted line) and measured (solid line) EM data. Lower panel: resistivity-depth pseudo-section and flight altitude (dotted line).

The same data was then inverted using magnetic half-space model. The initial value of the susceptibility was 0.001 SI. The fit between measured and computed data and the pseudo-sections of the (apparent) resistivity and magnetic susceptibility are shown in Figure 4. To reduce ambiguity, the susceptibility was set free only at those points for which the in-phase component was below a threshold value of 10 ppm. Figure 4 shows that AEM data is now well fitted also for the negative in-phase values. The basement is slightly more conductive for the magnetized parts of the profile when susceptibility of the basement is included in the inversion. The magnetic susceptibility has quite little variation along the profile. The depth to the top of the half-space is now greater although it is still located mostly above the ground level. Because the depth is unrealistically close to the flight path the values of magnetic susceptibility are underestimated.

The data was then inverted using a magnetic two-layer conductivity model. The initial resistivity and thickness of the overburden were 10000 Ωm and 50 m, respectively, and initial basement resistivity and susceptibility were the same as before. Because the depth to the top of the overburden was kept fixed (equal to the flight altitude), the model is now restricted below ground level. The inversion results for the AEM data and the resistivity pseudo-section are shown in Figure 5. Comparison to Figure 4 shows that the data is fitted equally well, but the basement is more resistive for the magnetized parts of the profile. The overburden layer is mostly rather resistive. Most of the deep conductors are overlain by very resistive overburden; a situation which resembles one-layer inversion in Figure 3. The two parts of the profile between distances 12–17 km are now overlain by conductive overburden and the basement is more resistive than in Fig-

ure 3. Because of the equivalence of the resistivity and thickness, the thickness of the overburden is likely to be overestimated and resistivity overestimate but the conductance is probably well resolved.
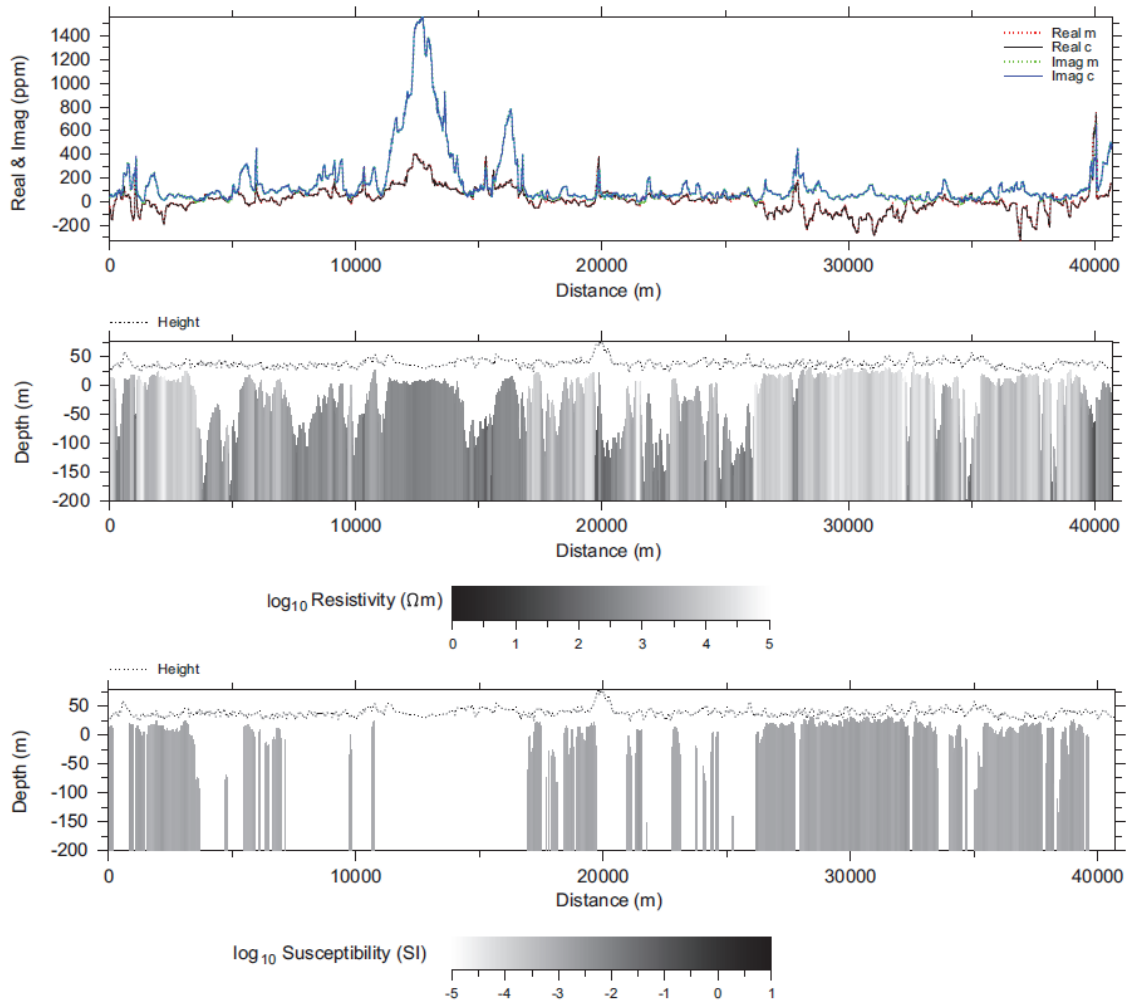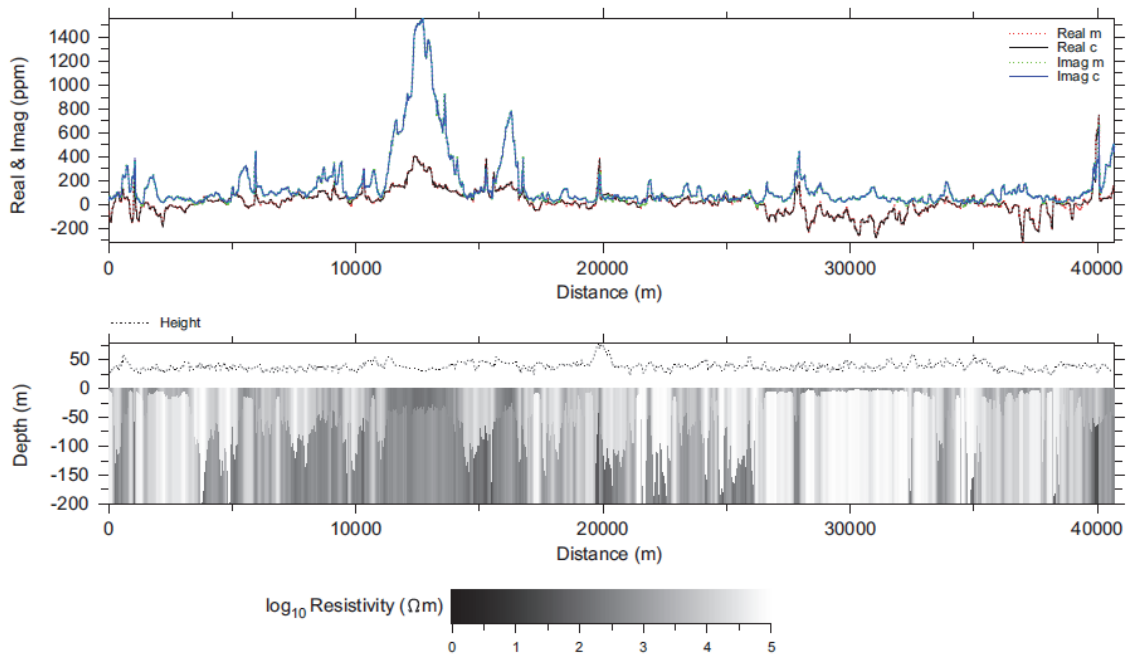

Fig. 4. Inversion results for the magnetic conductive half-space model. Upper panel: in-phase (real) and quadrature (imag) components of the measured (dotted line) and measured (solid line) EM data. Middle panel: resistivity-depth pseudo-section and flight altitude (dotted line). Lower panel: susceptibility-depth pseudo-section and flight altitude.

Fig. 5. Inversion results for the magnetic two-layer conductivity model, part 1. Upper panel: in-phase (real) and quadrature (imag) components of the measured (dotted lines) and computed (solid lines) EM data. Lower panel: resistivity-depth pseudo-section and flight altitude (dotted line).

The upper panel in Figure 6 shows the fit between the measured magnetic field (dotted red line) and the computed magnetic field (solid black line) resulting from the two-layer AEM inversion in Figure 5. The dotted black line represents the regional magnetic field which is defined by a spline function going through the automatically defined and evenly spaced knot points along the profile. The lower panel in Figure 6 shows the susceptibility pseudo-section below the profile. The susceptibility variation along the profile is bigger than in Figure 4, because the depth to the top of the basement is forced to locate below ground level. Figure 5 shows that most of the magnetic anomalies coincide with negative in-phase component values. Some magnetic anomalies have not been fitted at all because the in-phase component is above the 10 ppm threshold and, hence, the susceptibility of the corresponding part of the model is fixed to the initial value. Note that the fixed susceptibility values which were left out from Figure 4 are represented in Figure 5 by blue colour that matches the initial value of 0.001 SI. The amplitude of the computed magnetic anomalies are notably smaller than the measured field indicating that the susceptibility values obtained from the AEM inversion are still underestimated.

In order to fit the magnetic data better we then apply the new combined inversion method. The results are shown for the magnetic field and susceptibility in Figure 7. The intensity of the inducing magnetic field (52011 nT) and its inclination (75°) and declination (7°) are based on the IGRF model. The fit between measured and computed magnetic field is very good and the variation of susceptibility is much higher than in AEM inversion examples. Unfortunately, the inversion in Figure 7 was made with fixed knots.

As a consequence, the magnetic susceptibility is overestimated over large parts of the profile.
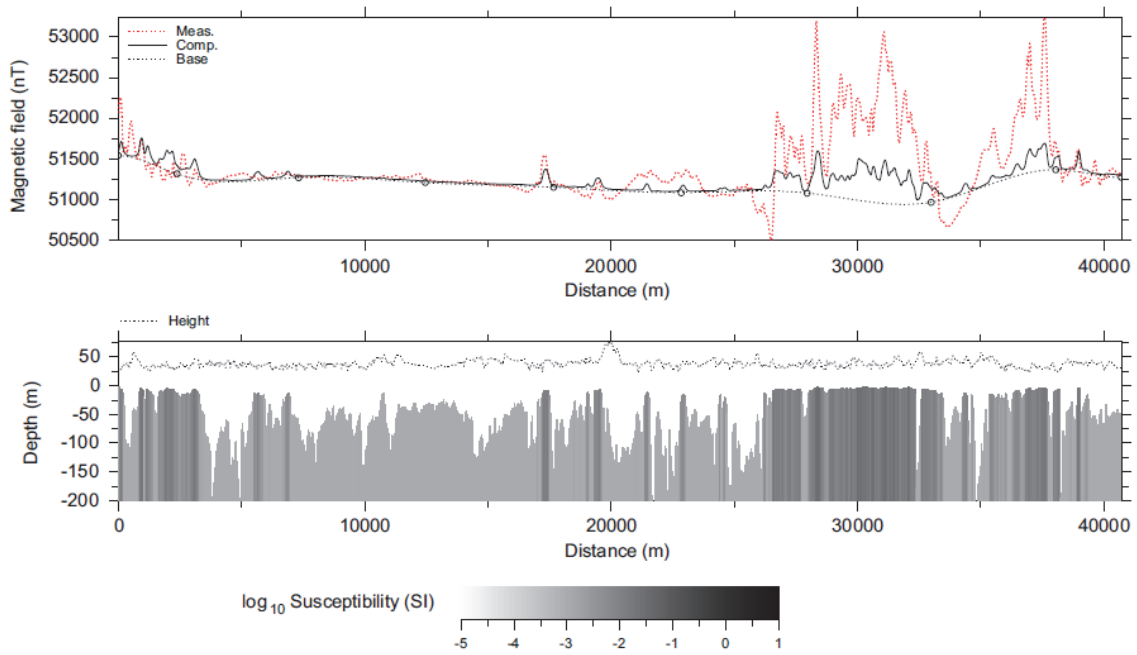

Fig. 6. Inversion results for the magnetic two-layer conductivity model, part 2. Upper panel: measured (dotted red line) and computed (solid black line) magnetic field and the spline representing the regional field (dotted black line). Lower panel: susceptibility-depth pseudo-section and flight altitude (dotted line).
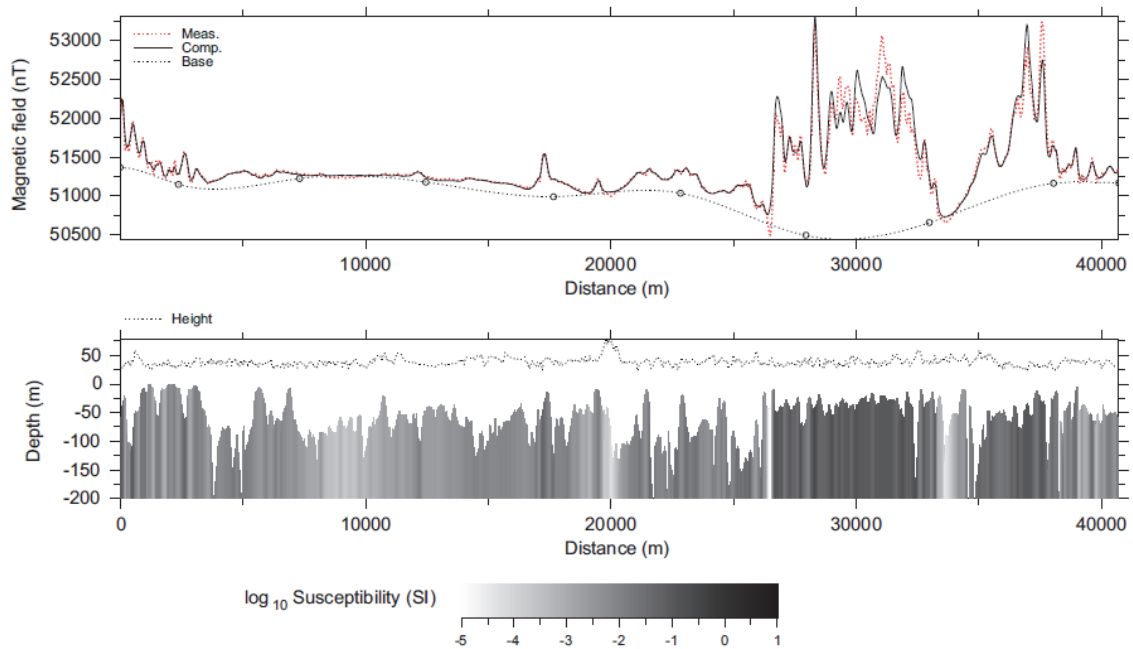

Fig. 7. Joint inversion results for the magnetic two-layer conductivity model without regional field optimization. Upper panel: measured (dotted red line) and computed (solid black line) magnetic field and the spline representing the regional field (dotted black line) Lower panel: susceptibility-depth pseudo-section and flight altitude (dotted line).

To adjust the regional field the knots need to be optimized during the inversion. For simplicity, this is done as a separate process between inverse iterations of the two-layer model parameters. The inversion results for the magnetic two-layer conductivity model are shown in Figures 8 and 9. The fit between measured and computed AEM data (upper panel in Figure 8) is as good as in Figure 5 but the depth to the basement layer is greater especially above the magnetic anomalies. This happens possibly because the inversion needs to give quite high susceptibility for the magnetized targets and such large values of susceptibility would affect the in-phase component too much unless the basement layer is put at a greater depth. Another reason is that AEM data is fitted using 1D layered earth model whereas magnetic field is interpreted using 3D vertical prism model. Although the thickness of the overburden is overestimated its conductance is likely to be resolved better.
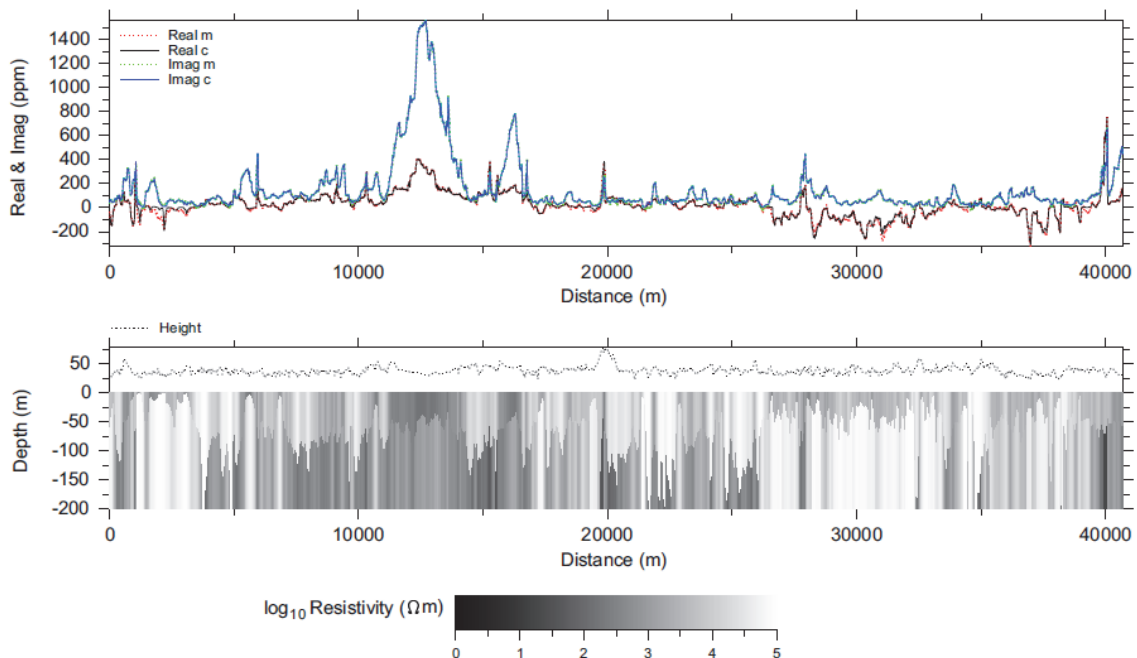

Fig. 8. Joint inversion results for the magnetic two-layer conductivity model with regional field optimization, part 1. Upper panel: in-phase (real) and quadrature (imag) components of the measured (dotted lines) and computed (solid lines) EM data. Lower panel: resistivity-depth pseudo-section and flight altitude (dotted line).

Figure 9 shows that the fit between measured and computed magnetic field is more-or-less as good as in Figure 7 but the regional field follows the long wavelength trend of the magnetic field better and hence the susceptibility is resolved better than in Figure 7 especially over the distance range 4–26 km.

3.2   Single map sheet

To investigate the performance of the new combined inversion method in a larger scale, the map sheet of Nivala (#2344) of size 30 km by 30 km is considered in the second example. Figure 10 depicts a background map and a lithological map of Nivala in

Northern Ostrobothnia region. Kalajoki river flows through the area from Haapajärvi in the SE corner towards Nivala in NW corner. Geologically the area is dominated by mica gneisses and mica schists that contain black schists.
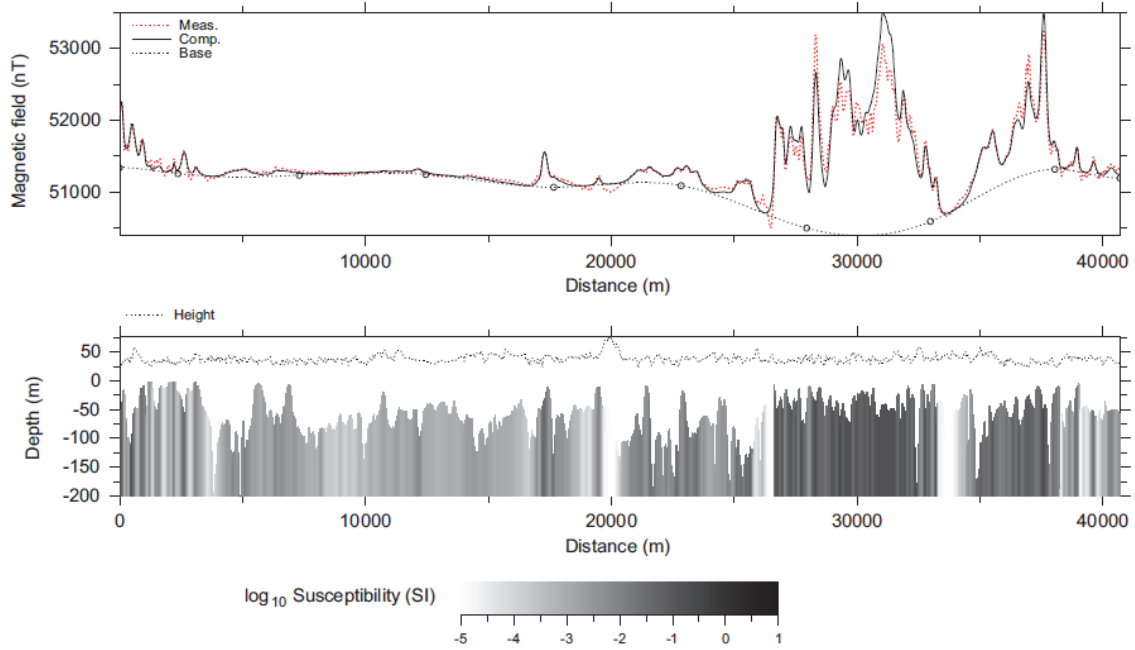

Fig. 9. Joint inversion results for the magnetic two-layer conductivity model with regional field optimization, part 2. Upper panel: measured (dotted red line) and computed (solid black line) magnetic field and the spline representing the regional field (dotted black line) Lower panel: susceptibility-depth pseudo-section and flight altitude (dotted line).
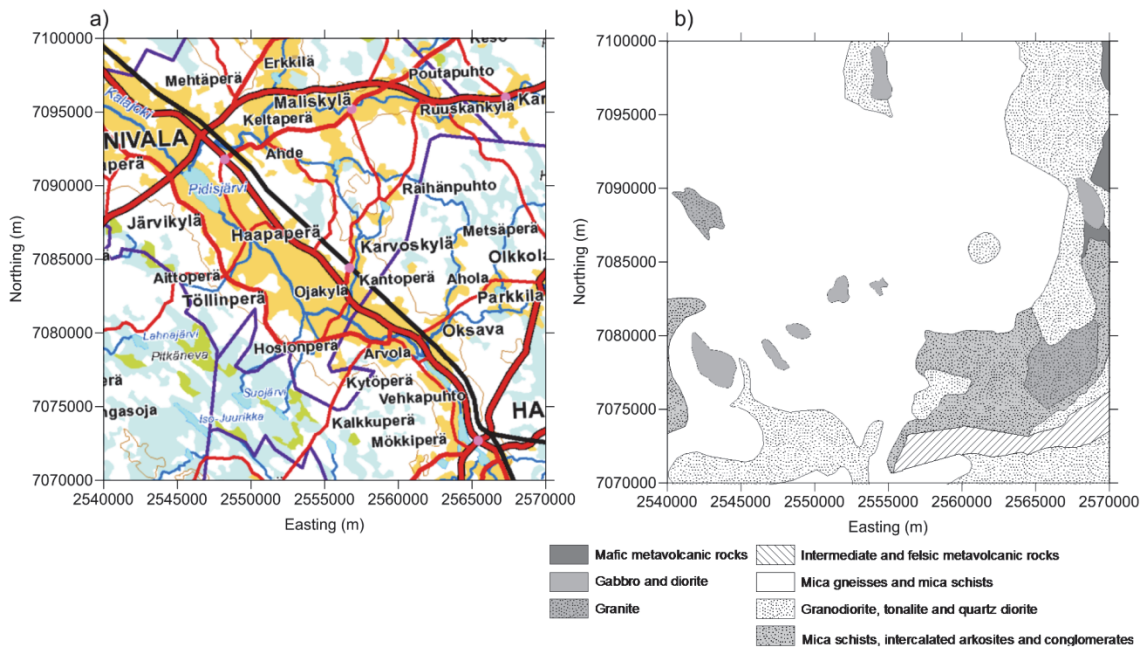

Fig. 10. Background maps for Nivala: a) base map in a scale of 1:500000 (National Land Survey © 2013) and b) geological map based on the lithological map of Finland of scale 1:1 million (Geological Survey of Finland © 2009). The coordinates are in the old national coordinate system of Finland (KKJ).

The AEM and magnetic data for Nivala are shown in Figure 11. The area was measured in 1980 using Twin Otter system. The data consists of 238 flight lines with 323227 sample points. The nominal line spacing and flight altitude of the EW directed lines are 200 m and 30 m, respectively. Figure 11c shows that flight altitude has been over 50 m over the two main power lines and above Nivala and Haapajärvi population centres and Hitura mine (at coordinates 2552000,7084000). The strongest anomalies in quadrature component (Fig. 11b) follow Kalajoki, Malisjoki and Settijoki rivers indicating that the river valleys are filled with conductive sediments. The strongest in-phase anomalies at the centre of the map are due to black schists.

The two-layer inversion was made in 10 iterations that took about two hours to compute on a PC with Intel i5 2500K processor. To compare the results against traditional apparent resistivity AEM inversions using a homogeneous (non-magnetic and magnetic) half-space model were also computed. Because of the simpler problem 10 iterations with one-layer model took only about an hour on the same computer.

Figure 12 shows the AEM inversion results for a homogeneous half-space model without and with magnetic properties. Figure 12a is more-or-less equivalent to an apparent resistivity map obtained applying transform table methods. Comparison between the two maps in Figure 12 shows that incorporation of magnetic susceptibility has decreased the resistivity of the least conductive areas. In both maps, however, the river valleys show up as moderately conductive (c. 100 Ωm) zones. Figure 12b shows less artefacts due to the EW flight direction.

The results of the two-layer combined inversion are shown in Figure 13. Comparison to Figure 12 shows how the two-layer inversion has succeeded in separating the conductive sediments of Kalajoki and other rivers. Consequently, the resistivity map in Figure 13d can be considered to represent the true resistivity of the bedrock better than the apparent resistivity based on homogeneous half-space. The thickness of the overburden is likely to be highly overestimated especially in areas where both the overburden layer and the basement are resistive. The conductance in Figure 13b, however, is resolved better and it can be used to investigate present and past river sediments and possible glacial features. The cumulative skin depth in Figure 13e is a useful side product of the inversion which resembles the basement resistivity map a lot. The skin depth can also be used to assess the reliability of the inversion. If the thickness of the overburden is greater than the skin depth the overburden cannot be considered to be well resolved.
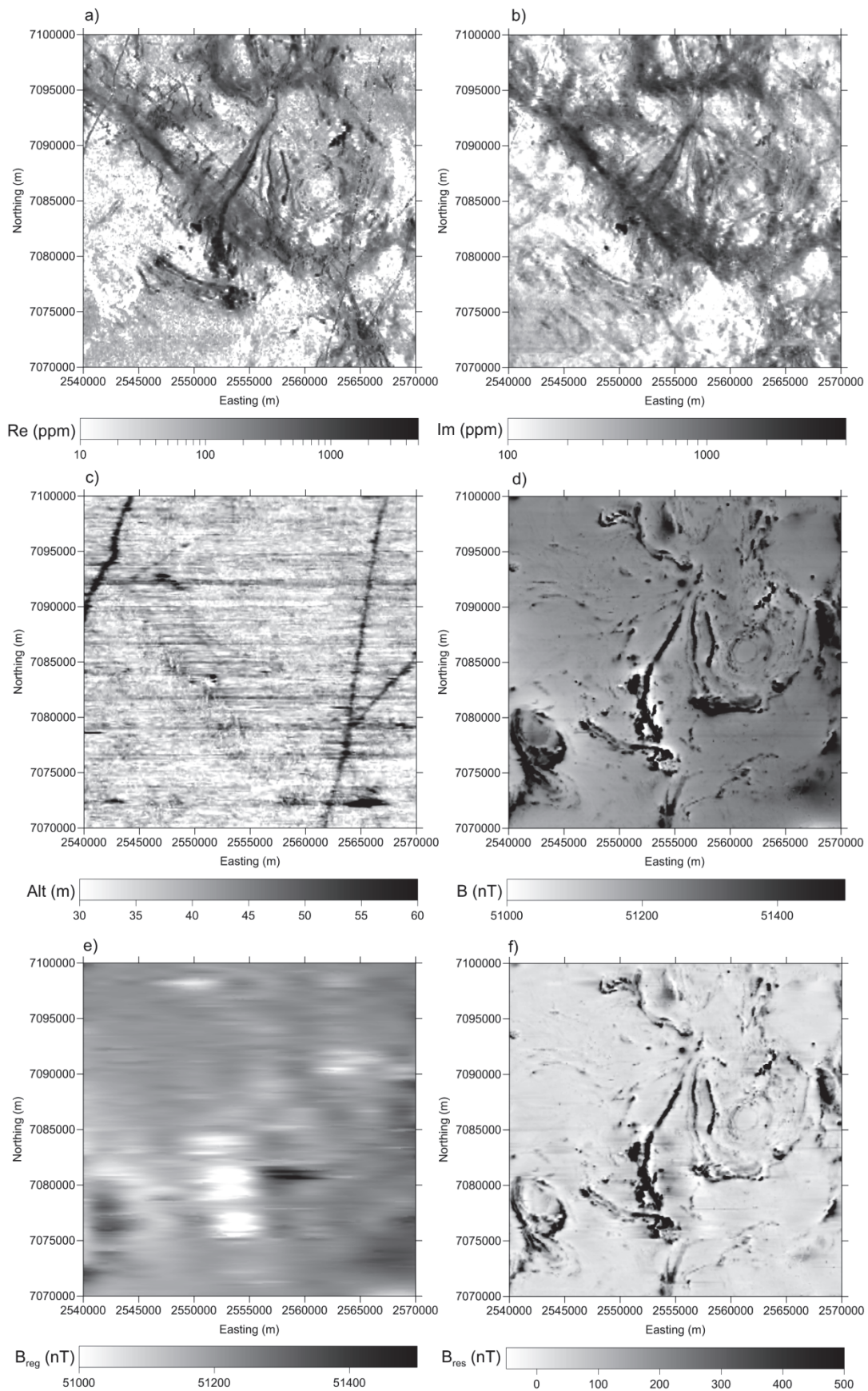
Fig. 11. Airborne geophysical maps of Nivala: a) in-phase component (Re), b) quadrature component (Im), c) flight altitude (Alt), d) measured magnetic field (B). The coordinates are in the old national coordinate system of Finland (KKJ).
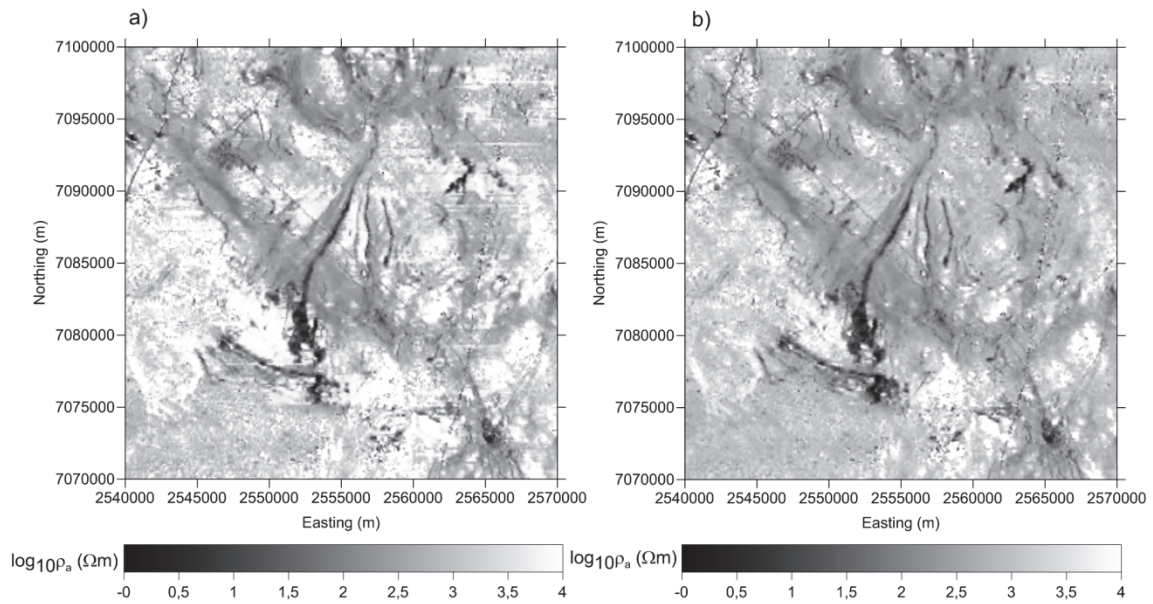
Fig. 12. Maps of AEM inversion results for Nivala using a) non-magnetic and b) magnetic conductive half-space model. The coordinates are in the old national coordinate system of Finland (KKJ).

The magnetic susceptibility map in Figure 13f resembles the magnetic map in Figure 11d, but lacks the long wavelength part totally. To some degree this makes it easier to follow and compare the level of the anomalies inside the map sheet. However, the susceptibility map shows some artefacts. In particular, the zones of high magnetic susceptibility (red and yellow) seem to be surrounded by zones of low susceptibility (dark blue). One of the reasons for this is the level of the regional base field and the initial susceptibility value (0.001 SI). To invert the data better the initial value of susceptibility should have been much smaller to mimic non-magnetic medium. Unfortunately, due to slow convergence many additional iterations and time would have been needed for good fit. In this example, however, the focus is on inversion of resistivity data and not on magnetic inversion, and hence, the background level of susceptibility will be overestimated. Another reason for the artefacts is that the magnetic data are not interpreted using a fully 3D model, and hence, the inversion yields apparent susceptibility values. For better magnetic interpretation the adjacent profile lines should have been taken into consideration.

Figure 14a depicts the regional magnetic field obtained as a side product of the two-layer inversion. The regional field shows EW directed smearing which suggests that the regional field should have been implemented so that the neighbouring profile lines were taken into account. This, however, would require a different kind of inversion approach where gridded AEM and magnetic data is used instead of profile data. The residual magnetic field in Figure 14b was computed by subtracting the regional field in Figure 14a from the measured magnetic field in Figure 11d. As such the residual field represents that part of the magnetic field that was actually inverted by the magnetic prism model. The residual field shows some EW directed stripes which are direct consequence of badly defined regional field.
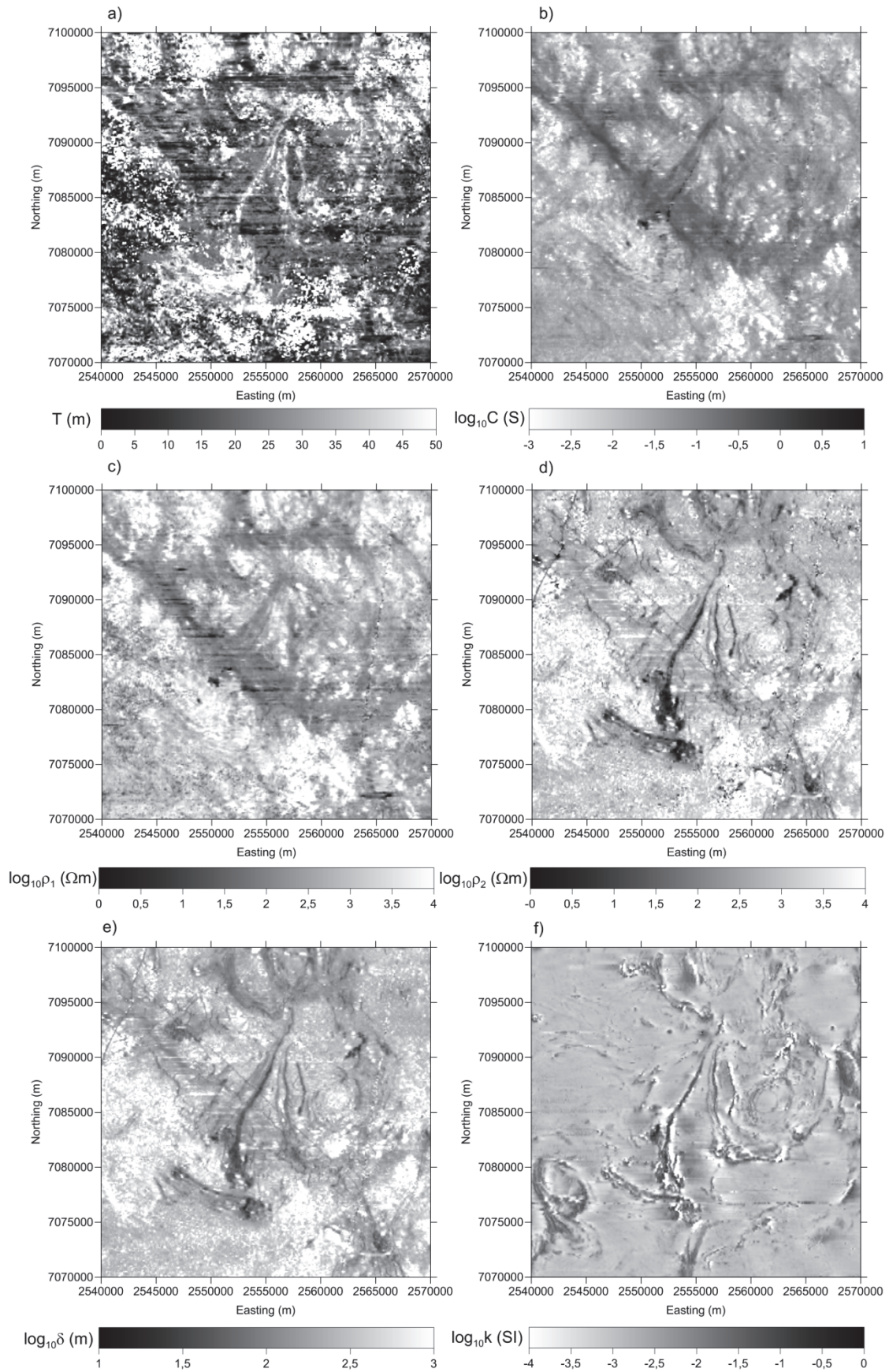
Fig. 13. Maps of combined inversion results for Nivala, part 1: a) overburden thickness, b) overburden conductance, c) overburden resistivity, d) basement resistivity, e) cumulative skin depth, and f) basement susceptibility. The coordinates are in the old national coordinate system of Finland (KKJ).
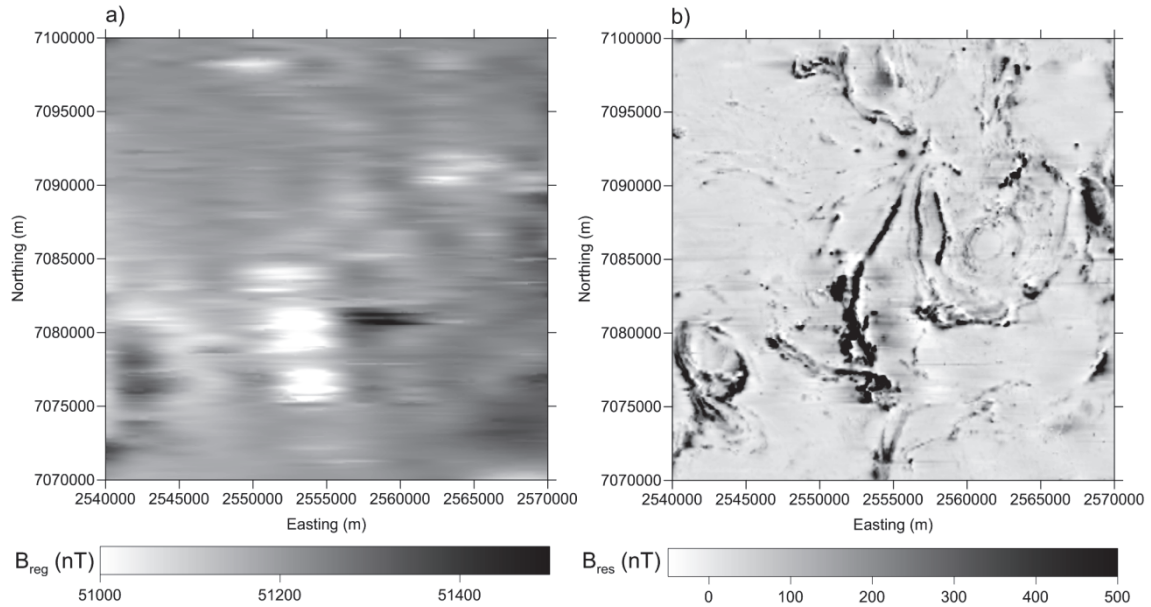
Fig. 14. Maps of combined inversion results for Nivala, part 2: a) the regional magnetic field (B_{reg}) obtained from two-layer inversion, and b) residual magnetic field ($B_{res}=B-B_{reg}$). The coordinates are in the old national coordinate system of Finland (KKJ).

4   Discussion and conclusions

The transformation methods based on conductive half-space model yield an almost unique solution for the apparent resistivity (and depth), whereas the two-layer inversion is also affected by the choice of the initial model (resistivity, susceptibility and thickness values), computational parameters (Lagrange scaler), and data and parameter weighting. The inversion results must be checked, and if the fit is poor, additional inverse iterations need to be made and inversion parameters and initial model may need to be changed. Sometimes the data quality may cause the problems (e.g. bad data, outliers, and missing data) and data needs to be edited manually.

The two-layer model itself has some limitations. Firstly, because of the limited frequency range the depth of penetration may not be sufficient if the overburden layer is too thick and too conductive. In this case the basement resistivity is likely to be too low and the conductance will be too small. Alternatively, the contrast between overburden and basement may not be sufficiently high to yield reliable estimates for overburden thickness. Thus, the inversion results require further analysis by the user. For example, the overburden thickness should be considered reliable only if the layer thickness is smaller than the skin depth and the resistivity contrast between the top and bottom layers is sufficiently high. Secondly, sharp maxima and minima in magnetic data can distort the spline interpolation of the regional magnetic field and its optimization.

The proper definition of regional field is the biggest problem in magnetic data inversion. Better processing of magnetic data would require the use of gridded data and two-dimensional interpolation for the regional field knots. This would also call for 2-D lateral constraining of the model parameters and 3-D modelling of the magnetic field. Furthermore, if remanent magnetization is associated with a low resistivity target there

will be a magnetic anomaly but no negative in-phase anomaly. To compensate for the (misleadingly) high magnetic susceptibility, the depth to the basement will be overestimated.

Finally, as *Huang and Fraser* (2000) have pointed out, the sources of conductivity and magnetic anomalies may not be the same. In other words, the depth to the top of magnetized sources may not be the same as the thickness of the overburden. This is also due to the smaller footprint of the AEM system than that of magnetic measurements. More advanced method to determine the optimal distance between the knots defining the regional field may be needed. Alternatively, a three-layer model, where the bottom layer is permeable and the resistivity of the middle layer and the basement are the same, could provide a solution for this problem.

Despite its problems and limitations, the two-layer AEM inversion can yield more reliable maps of apparent resistivity for the Finnish bedrock. More importantly, the combined inversion of AEM and static magnetic field data enables cross-correlation of the location and depth of conductive and magnetic anomaly sources.

Acknowledgements

References

Bhattacharyya, B.K., 1964. Magnetic anomalies due to prism-shaped bodies with arbitrary polarization. *Geophysics*, **29**, 517–-531.

Beard, L.P., 2000. Comparison of methods for estimating earth resistivity from airborne electromagnetic measurements. *J. of Appl. Geoph*, **45**, 239-259.

Christensen, N.B., 1990. Optimized fast Hankel transform filters. *Geoph. Prospecting*. **38**, 545–568.

Fraser, D.C., 1978. Resistivity mapping with an airborne multicoil electromagnetic system. *Geophysics*, **43**, 144–172.

Hautaniemi, H., M. Kurimo, J. Multala, H. Leväniemi and J. Vironmäki, 2005. The "three-in-one" aerogeophysical concept of GTK in 2004. In: Airo, M.-L. (ed.) Aerogeophysics in Finland 1972-2004, methods, system characteristics and applications. Geological Survey of Finland, Special Paper 39, 21–74.

Hjelt, S.-E., 1972. Magnetostatic anomalies of dipping prisms. *Geoexploration*, **10**, 239–254.

Hohmann, G.W. and A.P. Raiche, 1988. Inversion of controlled-source electromagnetic data. In: Nabighian, M.N. (Ed.) Electromagnetic methods in applied geophysics, **Volume 1**, Theory. Soc. of Expl. Geophys., 469–503.

Huang, H. and D.C. Fraser, 1998. Magnetic permeability and electric resistivity mapping with a multifrequency airborne EM system. *Expl. Geophysics*, **29**, 249–253.

Huang, H. and D.C. Fraser, 2000. Airborne resistivity and susceptibility mapping in magnetically polarizable areas. *Geophysics*, **65**, 502–511.

Huang, H. and D.C. Fraser, 2003. Inversion of helicopter electromagnetic data to a magnetic conductive layered earth. *Geophysics*, **68**, 1211–1223.

Korhonen, J.V., 2005. Airborne magnetic method: special features and review on applications. In: Airo, M.-L. (ed.) Aerogeophysics in Finland 1972-2004, methods, system characteristics and applications. Geological Survey of Finland, Special Paper 39.

Leväniemi, H., D. Beamish, H. Hautaniemi, M. Kurimo, I. Suppala, J. Vironmäki, R.J. Cuss, M. Lahti and E. Tartaras, 2009. The JAC airborne EM system: AEM-05. *J. of Appl. Geophysics*, **67**, 219–233.

Parasnis, D.S., 1979. Principles of applied geophysics. (3rd Ed). Chapman and Hall.

Peltoniemi, M., 1982. Characteristics and results of an airborne electromagnetic method of geophysical surveying. Geological Survey of Finland, Bulletin 321, 229 pp.

Pirttijärvi, M., 1995. TRANSAEM. Fortran-77 program to transform AEM data of GTK into apparent conductivity and depth. Geological Survey of Finland, Report Q17.9/95/1 (in Finnish).

Pirttijärvi, M., R. Pietilä, A. Hattula and S.-E. Hjelt, 2002. Modelling and inversion of electromagnetic data using an approximate plate model. *Geoph. Prosp.*, **50**, 425–440.

Pirttijärvi, M., 2003. Numerical modeling and inversion of geophysical electromagnetic measurements using a thin plate model. *Acta Univ. Ouluensis*, **A403** (PhD thesis).

Press, W.H., B.P. Flannery, S.A. Teukolsky and W.T. Vetterling, 1988. Numerical recipes, the art of scientific computing. Cambridge University Press.

Suppala, I., H. Vanhala and P. Lintinen, 2008. The dual frequency fixed-wing airborne EM system in delineating sulphide rich fine-grained sediments in Western Finland. AEM2008, 5th international conference on airborne electromagnetics, 28–30 May 2008. Haikko Manor, Finland, 4 p.

Ward, S.H. and G.W. Hohmann, 1988. Electromagnetic theory for geophysical applications. In Nabighian, M.N. (Ed.): Electromagnetic methods in applied geophysics, **Volume I** (Theory). Soc. of Expl. Geophys., 131–311.